Article:
Jones, KM, Milkiewicz, JA, Whitaker, JBC et al. (2 more authors) (2013) Photodissociation of ClNO in the 2 1A' state: computational and experimental NO product state distributions. Chemphyschem, 14 (7). 1479 - 1487. ISSN 1439-4235

https://doi.org/10.1002/cphc.201200999

Photodissociation of ClNO on the 2 ^{1}A′ state: computational and experimental NO product state distributions

KM Jones, JA Milkiewicz, BJ Whitaker, * AG Sage, †
and GA Worth ‡

November 2012

1 Abstract

The ultrafast photodissociation of the 2 ^{1}A′ state of ClNO, which has an absorption spectrum peaking at 335 nm, has been studied using computational and experimental methods. New potential energy surfaces have been calculated for the 1 and 2 ^{1}A′ states at the MRCI level. Wavepacket dynamics simulations have been performed both exactly and using the Multi-Configuration Time Dependent Hartree method, yielding essentially identical results. Transition dipole moments at a range of geometries have been included in these calculations to correctly model the excitation. Product NO vibrational and rotational state distributions have been obtained both computationally by analysing the quantum flux on the 2 ^{1}A′ surface and experimentally by use of 3D REMPI, a variant of the velocity map imaging technique. The nascent NO is found to be only marginally vibrationally excited, with 91% formed in v=0. The calculated NO rotational distribution peaks in the j=45-55 region, comparing favourably to experiment.

2 Introduction

The photodissociation of nitrosyl chloride, ClNO, has been studied as a prototypical example of bond rupture since the 1930s.[1] In the UV-vis region (2 to 7 eV) ClNO exhibits strong absorption and readily dissociates to give NO and Cl products in their ground electronic states. The NO can be formed in a variety

*corresponding author: School of Chemistry, University of Leeds, Leeds LS2 9JT, UK.Fax: +44 (0)113 343 6565; Tel:+44 (0)113 343 6543; E-mail: b.j.whitaker@leeds.ac.uk
†Current address: School of Chemistry, University of Bristol, Bristol, UK.
‡School of Chemistry, University of Birmingham, Birmingham, UK.

of vibrational and rotational states depending on the photon energy and hence the excited electronic state accessed.[2] With only 32 electrons it is amenable to computational study using *ab initio* methods. As an easily-prepared, albeit highly corrosive, gas it is also convenient for detailed experimental investigation by techniques such as velocity map imaging. ClNO is also of interest to the atmospheric chemistry community, being a source of radical Cl particularly in urbanised regions of the coast.[3] A further motivation for revisiting the photochemistry of this molecule from a computational perspective is the possibility of using it as a target molecule for coherent control experiments through optical pulse shaping.[4, 5]

ClNO belongs to the C_s point group and hence its electronic states are of either A' or A'' symmetry. Ignoring spin-orbit coupling, there are 12 states which correlate to the ground electronic states of NO and Cl ($^2\Pi$ and ^2P respectively) on dissociation: $3 \times {}^1A'$, $3 \times {}^1A''$, $3 \times {}^3A'$ and $3 \times {}^1A''$. All of these barring the $1\ {}^1A'$ are dissociative, but there is some variation in their lifetimes, with the $1\ {}^1A''$ and $1\ {}^3A''$ in particular existing long enough to exhibit structured absorption bands.[6, 7, 8] For the $2\ {}^1A'$ state of interest here the dissociation process is over more quickly, but the topology of the potential energy surface (PES) still has a marked influence upon the NO product state distribution.

The $2\ {}^1A'$ state absorbs light between 280 and 400 nm (3 to 4.5 eV) with a peak at 335 nm (3.72 eV).[9] It is commonly referred to in the literature as the B band following the nomenclature introduced by Goodeve and Katz.[10] The exact identity of the state giving rise to this band was uncertain for some time, despite early calculations[11] and experimental work showing that it was of A' symmetry.[12, 13] The problem was solved when Reisler and co-workers conducted photofragment yield spectroscopy experiments[9, 13] which confirmed the symmetry and showed it gave rise to NO fragments primarily in the $\Pi(A'')$ Λ-doublet state. In a Hartree-Fock molecular orbital model this implied excitation was to an orbital perpendicular to the plane of the molecule. Combining this information with *ab initio* calculations showed clearly that the $2\ {}^1A'$ state was responsible, with the primary excitation being from the Cl p_z orbital to a NO $\pi_z{}^*$ antibonding orbital. This assignment was further confirmed by later, more advanced calculations.[14, 15]

Reisler's experiments also revealed the NO (v=0) rotational distributions following photodissociation at 355 nm. These were found to be bell shaped, peaking at $j{\sim}46$ [13] or $j{\sim}43$[9], where j is the rotational quantum number of the NO nuclear frame. More recent, detailed state-selected experiments carried out by Torres *et al.* found a similar narrow distribution peaking at j=46 for NO in its ground vibrational state.[16] This high level of rotational excitation implies anisotropy on the excited state surface, an observation borne out by previous calculations of the $2\ {}^1A'$ surface.[15]

In this article vibrational and rotational distributions in the NO fragment following dissociation on the $2\ {}^1A'$ surface are calculated and compared to experimental distributions measured using the 3D REMPI technique. The article also sets the foundation for forthcoming work on ClNO excited state surfaces including spin-orbit coupling, and on coherent control through optical pulse

shaping.

3 Methodology

3.1 Potential energy surfaces

All electronic structure calculations were carried out using the MOLPRO 2010 package.[17] Firstly, potential energy surfaces (PESs) for the 1 and 2 ^{1}A$'$ states were constructed. 2464 *ab initio* points were calculated across the following binding coordinates:

rNO: every 0.2 bohr from 1.75 to 2.95
rClN: every 0.25 bohr from 2.75 to 6.0, then every 0.5 bohr to 10.0
bond angle θ: every 10° from 20° to 170°.

The initial orbitals were obtained using the CASSCF method[18, 19] state-averaged over the first 3 states of ^{1}A$'$ character. A full valence active space was used, with the N and O 1s and Cl 1s, 2s and 2p orbitals kept doubly occupied but not frozen. For rClN values greater than 6.0 bohr the occupation of the molecular orbital corresponding to the Cl 3s atomic orbital had to be restricted to 2 in order to prevent erroneous orbital re-ordering.

The CASSCF orbitals were then used to calculate the 1 and 2 ^{1}A$'$ states using the MRCI (single and double excitations) method.[20] The contribution of quadruple excitations to the overall energy was estimated by the Davidson correction using relaxed reference functions. All generated configuration state functions were included. For these calculations the Dunning augmented correlation consistent polarised valence quadruple zeta (aug-cc-pVQZ) basis set was used.

Although alternative fitting functions were investigated, the quality of the *ab initio* points was sufficiently good that the surfaces could be smoothly fitted using 3D cubic splines. The resultant surfaces were used for dynamics calculations.

3.2 Wavepacket dynamics methods

The majority of the quantum dynamics calculations were performed using the Multi-Configuration Time Dependent Hartree method (MCTDH) [21, 22] as implemented in the Heidelberg software package.[23] Although ClNO is a small molecule and can be treated by exact calculations with relative ease, the MCTDH method was chosen to allow many wavepacket propagations to be run rapidly with very little loss of accuracy, and also to allow the full functionality of the suite of analysis programs to be utilised. A full description of the MCTDH method is given in ref. [24].

Briefly, the MCTDH wavefunction is written as a sum of Hartree products, in which each degree of freedom is represented by single particle functions (SPFs).

These SPFs are time-dependent basis functions, wherein lies the strength of the method: if the functions are allowed to adapt during a wavepacket propagation fewer are needed for an accurate description of the dynamics. The underlying equation of the MCTDH method is:

$$\Psi(Q_1, ..., Q_f, t) = \sum_{n_1}^{j_1=1} ... \sum_{n_f}^{j_f=1} A_{j_1 ... j_f}(t) \times \prod_{\kappa=1}^{f} \varphi_{j_\kappa}^{(\kappa)}(Q_\kappa, t) \tag{1}$$

where the $Q_1, ..., Q_f$ are the nuclear coordinates, the $A_{j_1 ... j_f}$ are the expansion coefficients and the $\varphi_{j_\kappa}^{(\kappa)}$ are the SPFs for each degree of freedom κ. When more than one PES is included in the calculation multiple, distinct sets of these SPFs can be used.

Each SPF comprises a linear combination of time-independent functions known as the primitive basis. The form of the primtive basis functions is dependent upon the nature of the corresponding degree of freedom. To improve computational efficiency the Discrete Variable Representation (DVR) is used for these, allowing the wavefunction to be localised onto a grid.[25] In this work, a Legendre DVR has been chosen for the angular coordinate, with a sine DVR (using the particle-in-a-box functions as its basis) for the dissociative coordinate and a harmonic oscillator (HO) DVR for the bound coordinate.

Although the PESs have been calculated using binding coordinates, in the dynamics calculations they were converted to the Jacobi scattering coordinates shown in Figure 1. The main advantage of this coordinate system is that it leads to a considerable simplification of the kinetic energy operator. For systems where the total angular momentum is taken to be zero (an approximation used throughout in this work), the operator is:

$$\hat{T}(R, r, \gamma) = -\frac{\hbar^2}{2\mu_R}\frac{\partial^2}{\partial R^2} - \frac{\hbar^2}{2\mu_r}\frac{\partial^2}{\partial r^2} - \frac{1}{2}\left(\frac{1}{\mu_R R^2} + \frac{1}{\mu_r r^2}\right)\frac{1}{\sin\gamma}\frac{\partial}{\partial\gamma}\sin\gamma\frac{\partial}{\partial\gamma} \tag{2}$$

where μ_R and μ_r are the reduced masses for the R and r coordinates respectively.

After the PESs have been fitted by splines they are transformed into MCTDH product form using the POTFIT program from the Heidelberg MCTDH suite.[26, 27] This allows the entire Hamiltonian to be written as a sum of products of SPFs and so facilitates the calculation of the required integrals.

In the asymptotic region a Complex Absorbing Potential (CAP)[28, 29] is placed on the R coordinate in order to absorb the wavepacket. This function has the form:

$$-iW(R) = -i\eta\left(R - R_{cap}\right)^b h\left(R - R_{cap}\right) \tag{3}$$

where R_{cap} is the start point, η is the strength (set here to 0.3), b is set to 3 and $h(R - R_{cap})$ is a Heaviside step function. Without a CAP there is a danger that the wavepacket would hit the edge of the grid and either be reflected backwards or reappear at the opposite end of the PES. In addition, it is very useful as the quantum flux which passes into it can be recorded and subsequently analysed.

A standard method for obtaining product state distributions following wavepacket propagations is to take the time-dependent wavefunction in the asymptotic region and then project it onto the eigenstates of the individual product species. This can also be done by using the combination of the flux operator and the CAP, as outlined in ref. [30]. The flux operator $\hat{F}$ measures the quantum flux passing into the asymptotic region of the surface along the Jacobi R coordinate:

$$\hat{F} = \frac{i}{\hbar}[\tilde{H}, h(R - R_{cap})] \tag{4}$$

where R_{cap} is defined as before, and $\tilde{H} = \hat{H} - iW$ in order to include the CAP in the operator.

To calculate the scattering matrix from a ClNO photodissociation channel a into a NO product state b using this flux operator, the working equations are

$$|S_{NO_b,ClNO_a}(E)|^2 = \frac{2}{\pi|\Delta(E)|^2} Re \int_0^T g_{NO_b}(\tau) e^{iE\tau} \mathrm{d}\tau \tag{5}$$

and

$$g_{NO_b}(\tau) = \int_0^{T-\tau} \langle \Psi(t)|P_{NO_b} W P_{NO_b}|\Psi(t+\tau)\rangle \mathrm{d}t. \tag{6}$$

where T is the final propagation time, ΔE is the energy spread of the initial wavepacket, and P_{NO_b} is the projector onto the b state of NO. The form of the projector will vary depending upon the state in question. It is also possible to apply multiple projectors, for example to find out the amount of NO produced in a particular rotational state *and* a particular vibrational state.

In the exact calculations the wavepacket was propagated using the Short-Iterative Lanczos (SIL) method. In the MCTDH calculations the SIL method was used for propagating the expansion coefficients and the Bulirsch-Stoer extrapolation integrator was used for the SPFs.[24]

3.3 Velocity map imaging

Velocity map imaging (VMI) is a well established experimental methodology for recording quantum state selected product distributions following photodissociation.[31] Usually a nanosecond UV laser pulse is used to dissociate the molecule of interest and a second pulse subsequently probes the products by resonant multiphoton ionization (REMPI). The resultant ions are then detected on a position sensitive detector which, by virtue of the electrostatic lens used to extract them, provides a velocity (speed and direction) map of the state selected photo-products. In favourable circumstances a single laser pulse can act both to dissociate the target molecules and to ionize the desired photoproduct, which is the approach used here.

The apparatus used has been described elsewhere.[32, 33] Briefly, gaseous ClNO was prepared by mixing samples of Cl_2 and NO in a stainless steel cylinder

and back filling with He carrier gas. Typical samples consisted of ∼0.133 bar of Cl_2 and ∼0.266 bar of NO in 8.0 bar of He (∼5%). The sample at a backing pressure of a few bar is expanded into a vacuum chamber through a pulsed valve (Parker, Iota one, series 9) and the resulting molecular beam is skimmed by a 1 mm dia. skimmer (Molecular Beam Inc.) a few centimeters downstream of the valve where it enters the ionization chamber. The velocity map electrostatic lens is configured on axis. Photodissociation was initiated using a nanosecond laser pulse (Continuum Surelite II pumped Sirah stretch dye laser operating with pyridine 2 or styryl 8 and frequency doubled) at a wavelength in the 350 – 380 nm region.

The product NO was ionised by (2+1) REMPI via the D $^2\Sigma^+ \leftarrow$ X $^2\Pi$ or C $^2\Pi \leftarrow$ X $^2\Pi$ states using the same laser pulse. The frequency doubled output of the dye laser (*ca.* 5 mJ) was focused onto the molecular beam in the centre of the ion optics using a 250 mm fused silica lens. Using the two photon D $^2\Sigma^+ \leftarrow$ X $^2\Pi$ and C $^2\Pi \leftarrow$ X $^2\Pi$ transitions to detect NO has three advantages. Firstly, these transitions lie at convenient energies which allow photodissociation of the 2 ^{1}A′ state to be studied using a single laser experiment. Secondly, unlike the more usual (1+1) REMPI probe of NO via the A $^2\Sigma^+ \leftarrow$ X $^2\Pi$ band, the transitions are not easily saturated making it easier to quantify alignment effects. Thirdly, the Λ doubling of the NO(X $^2\Pi$) rotational states is easily spectrally resolvable in the C $^2\Pi \leftarrow$ X $^2\Pi$ band.

In order to gain a rapid overview of the rotational state product distribution and to easily discriminate between NO that might be present in the molecular beam as a contaminant from incomplete reaction or as a photoproduct of NO_2 dissociation (another potential contaminant species) the velocity resolved or 3D REMPI technique recently introduced by Dick and co-workers has been used.[34] In our version of the method the voltages of the VMI lens are adjusted for direct current (DC) slice-imaging[35] and the micro-channel plate detector is gated with a short (<10 ns) high-voltage pulse to only record a thin slice through the centre of the Newton sphere of state selected ions, as described in ref. [33].

Our image processing software (in-house code written in LabView) works by recording a series of controided images as a function of wavelength, which are subsequently post-processed. Recording only the centroid coordinates rather than the entire image at each wavelength considerably reduces the data storage requirements and typically a two nanometre wavelength scan with images recorded every 0.005 nm requires *ca.* 300 kb of disc space (compared to the 1 Gb or more needed for a sequence of uncompressed images). Radial integration of each of these images yields a 1D data array of intensity against pixel number (which is directly proportional to the velocity of the detected photofragment). Combination of many of these processed images as a function of wavelength yields a 3D 'map' of wavelength, velocity and intensity. A typical experimental scan involved accumulating data for 150 laser shots per wavelength step.

4 Results

4.1 Surfaces

4.1.1 1 ^{1}A′ surface

The 1 ^{1}A′, or S_0, surface is the ground state of the ClNO molecule. The minimum energy geometry calculated at the MRCI/aug-cc-pVQZ level is rClN=3.74 bohr and rNO=2.15 bohr with a bond angle θ of 113.4°. This is in very good agreement with the experimental optimum geometry of rClN=3.72 bohr, rNO=2.14 bohr and θ=113.4°.[36, 37]

The dissociation energy, obtained by taking the difference between the energies at the 1 ^{1}A′ minimum and out in the asymptotic region (using the same rNO and angular values but with rClN=20.0 bohr), is 1.619 eV. This again agrees very well with the experiment-based value of 1.615 eV.[38, 7]

A cut through the surface at a bond angle θ of 110° is given in panel a) of Figure 2. Note that the well is not uniform, but instead extends slightly into the rNO coordinate at lower rClN distances. In panel b) another cut is given for a rNO bond length of 2.15 bohr. The key features here are the two wells, with one at the Franck-Condon (FC) geometry and the other further out centred at around rClN=5.7 bohr, rNO=2.1 bohr and θ=40°, which corresponds to the ClON isomer.[39] This second well arises due to an interaction with the 2 ^{1}A′ state, occuring at around θ=70° throughout the surface. The states are extremely close in energy at this point from about rClN=5.75 bohr outwards for a rNO bond length of 2.15 bohr. A one-dimensional cut at rNO=2.15 bohr and rClN=6 bohr is given in Figure 3 to illustrate this. Work is underway to calculate the non-adiabatic coupling matrix elements between the 2 states in this region. Note it is rather unusual to find conical intersection seams in asymptotic regions and this may be of significance in discussions of roaming dissociation mechanisms.

4.1.2 2 ^{1}A′ surface

The calculated energy difference between the 1 and 2 ^{1}A′ states at the FC point is 3.704 eV, which is in good agreement with the experimental peak of the B band at 3.72 eV.[9] The energy difference between the dissociation asymptote and the FC point on the 2 ^{1}A′ surface is -2.085 eV.

Cuts through the 2 ^{1}A′ surface are given in Figure 4. Panel a) gives a cut at θ=110° which shows the considerable steepness of the slope from the FC to asymptotic regions. The cut in panel b) at rNO=2.15 shows clearly the kink at an angle of around θ=70° due to the intersection with the 1 ^{1}A′ state. In panel c), the equivalent cut plotted in Jacobi coordinates shows how the slope of the surface at the FC point points steeply towards smaller γ.

4.1.3 Transition dipole moments

The transition dipole moments (TDMs) between the two states were also calculated at each geometry at the MRCI level of theory. The TDMs as calculated using MOLPRO comprise two perpendicular in-plane components aligned along the eigenvectors of the inertia tensor matrix. This gives a body-fixed view. Here however instead of considering the two in-plane components separately they have been treated together by calculating their resultant.

The bulk of these resultants lie along the Jacobi R coordinate. This is expected as the excitation from the 1 ^{1}A$'$ to the 2 ^{1}A$'$ states involves promotion of an electron from a Cl $3p$ orbital to an NO π^* orbital. For example, at the FC point, the component of the TDM aligned in the same direction as the Jacobi R coordinate was 0.076 atomic units (au), and the component in the perpendicular coordinate was -0.0071 au. These FC values compare reasonably well with the results of previous calculations.[15]

Calculated TDMs are rarely reliable outside of the FC region. In this work, they were found to vary smoothly across a limited region of the PES, from approximately rClN=3.5 to 5.0 bohr and from θ=90° to 130°. Outside this region the TDMs were set to zero. Figure 5 gives an example cut, showing how the magnitudes of the TDMs vary with bond angle θ. The TDMs at each geometry were combined to create a 'surface', which was then converted to Jacobi coordinates and used in the dynamics calculations.

4.2 Wavepacket dynamics

Quantum dynamics calculations were carried out to obtain information about the dissociation process on the 2 ^{1}A$'$ state. The Hamiltonian used was simply

$$\hat{H_n} = \hat{T} + V_n\left(R, r, \gamma\right) \tag{7}$$

with $\hat{T}$ being the kinetic energy operator stated previously in Equation 2 and V_n being the PES for the desired state n. 288 grid points were used on the DVR in the R coordinate, 48 in the r coordinate, and 200 in the γ coordinate. Calculations were run both exactly and using the MCTDH method, with both approaches giving near-identical results. For the MCTDH calculations, which will be discussed here, 10 SPFs were used for each coordinate.

Firstly, the wavepacket was relaxed on the 1 ^{1}A$'$ surface to obtain the lowest energy eigenstate for the system. This was achieved by propagating the wavepacket in imaginary time, $i\tau$,[24] for a few tens of fs until there was no further change. Secondly, the wavepacket on the 2 ^{1}A$'$ surface was formed by operating on the relaxed 1 ^{1}A$'$ wavefunction using the TDM surface. Thirdly, the wavepacket on the excited state was allowed to propagate. A CAP was placed on the R coordinate at R=7.5 bohr to prevent reflection of the wavepacket from the edge of the grid.

Snapshots of the wavepacket every 10 fs as it propagates on the 2 ^{1}A$'$ surface are shown in Figure 6. As can be seen in the cut at γ=113° in panel a), the wavepacket receives only a small impetus in the NO coordinate as its

starting position is very close to the energy minimum. The NO product would therefore be expected to have little to no vibrational excitation. The cut at rNO=2.15 bohr given in panel b) is more interesting: the wavepacket is initially high on a steep wall angled towards lower γ, and so proceeds rapidly downhill in this direction. The NO product would therefore be expected to have significant rotational excitation.

One of the most basic, and yet most revealing, pieces of data that can be obtained from such calculations is the autocorrelation function:

$$c(t) = \langle \Psi(0) | \Psi(t) \rangle \tag{8}$$

The total absorption spectrum is obtained from the autocorrelation function via Fourier transformation:[40, 41]

$$\sigma(E) \propto \int e^{iEt} c(t)\, \mathrm{d}t \tag{9}$$

The autocorrelation function for this system is very simple: the wavepacket moves away from its initial postition very rapidly and there are no recurrences. This results in a broad, featureless absorption spectrum peaking at an energy of 3.79 eV (equivalent to 327 nm), as shown in Figure 7, which may be compared to the experimental spectrum of Goodeve and Katz[10] and the calculated spectrum of Yamashita and Kato.[15]

Further information can be obtained regarding product NO rotational and vibrational product state distributions by considering the quantum flux passing into the CAP, as discussed earlier. For the NO vibrational states it was first necessary to calculate the lone NO potential energy curve at the same level of theory as the ClNO PESs. The *ab initio* points were then fitted to an Extended Rydberg function of the form

$$V_{NO}(r) = -D_e \left(1 + \sum_{k=1}^{6} a_k \rho^k \right) e^{-b\rho} \tag{10}$$

where $\rho = r - r_e$. The value for r_e so obtained matches the experimental value of 2.18 bohr, and the value of 6.49 eV for the dissociation energy D_e is near-identical to the experimental value of 6.48 eV.[42] From this function the NO vibrational eigenstates could be found and then projected onto the asymptotic flux.

Figure 8 shows the flux passing into each NO vibrational state and Table 1 gives the proportion of the total flux going into each state for the whole range of energies contained in the initial wavepacket. The total flux distribution is, as would be expected, broad and featureless like the absorption spectrum (Figure 7). The flux distributions into the individual vibrational states are similarly-shaped, with the peaks shifted slightly in energy. The vast majority of NO is formed in v=0, with only 8% in v=1. The populations of higher excited states are negligible. The photodissociation process is therefore essentially adiabatic with respect to the NO stretch.

Interestingly, if TDMs are not employed in the initial excitation and the relaxed wavepacket is simply placed 'as-is' on the 2 ^{1}A$'$ state, the calculated NO vibrational distribution is different. As shown in Table 1, although most NO is still formed in v=0, the proportion in v=1 is more than doubled. This is because the TDM operator has the effect of shifting more wavepacket density closer to the minimum in the rNO coordinate, hence giving less impetus in the direction of longer rNO.

To find the NO rotational state populations the quantum flux was projected onto the spherical harmonics. This gives the flux distribution for each value of j, the NO rotational quantum number. Integrating these across all energies gives the overall NO rotational distribution, which is narrow and Gaussian-shaped. The peak is at j=51 and the full-width half-maximum (FWHM) is $\sim \Delta_j$=15. The product state distributions for a single energy, such as that for photodissociation using a nanosecond laser pulse, can be obtained from this one calculation by looking just at the flux results at that specific energy. Note that unlike those for NO vibration, the rotational distributions are unchanged by inclusion of the TDM operator in the calculation.

4.3 Imaging results

A full report of our '3D slice imaging' results will be published elsewhere. Here a subset of the data is presented in the form of velocity resolved REMPI spectra recorded between 369 and 379 nm where the laser wavelength spans a number of (two-photon) rotational transitions in the D $^2\Sigma \leftarrow$ X $^2\Pi$ (0,0) and C $^2\Pi \leftarrow$ X $^2\Pi$ (0,0) bands (Figure 9 panels a) and c)). The spectra shown are comprised of several shorter scans which have been 'stitched' together. This was done by normalising each scan to its neighbour using an overlap of between 0.1-0.5 nm.

In order to assign the 3D REMPI spectrum, the wavelengths of each of the possible rotationally resolved REMPI transitions were calculated from the well known spectroscopic constants of the D $^2\Sigma$, C $^2\Pi$ and X $^2\Pi$ states of NO.[43, 44] Once the quantum state of each transition was known, its expected velocity could be calculated (for NO(v=0)) using:

$$v(NO) = \sqrt{\frac{2 \times (E_{phot} - E_{rot} - E_{elec} - D_0)}{m_{NO}\left(1 + \frac{m_{NO}}{m_{Cl}}\right)}} \tag{11}$$

Here, $v(NO)$ is the velocity of the NO photofragment formed in a particular quantum state, E_{phot} is the photon energy, E_{rot} is the rotational energy of the NO fragment, E_{elec} is the spin-orbit electronic energy of the NO and Cl fragments, D_0 is the bond dissociation energy and m_{Cl} and m_{NO} are the masses of the Cl and NO fragments respectively. The data represented in this form closely resemble a Fortrat diagram, with a simple linear transformation being sufficient to convert the vertical axis of the spectrum from velocity to total angular momentum space (J).

As is evident from an inspection of panels a) and c) of Figure 9, the agreement between the measured and predicted speeds of the NO photofragments from

ClNO is very good. It is also immediately clear that the NO fragments are produced rotationally 'hot' and in a narrow distribution. From the intensities of the peaks in the speed map the rotational distributions can be extracted. This is done by applying appropriate Hönl-London factors for each of the branches to correct for the relative line strengths. These are calculated using PGopher[45], with a pure T[2,1] transition moment tensor for the D-X lines, and appropriate contributions from the T[0,0], T[2,0] and T[2,2] tensors for the C-X lines.

As this is a one-colour experiment the different rotational branches are probed at slightly different excitation, and hence photolysis, wavelengths. The branches for the C and D states of NO are therefore considered separately. Note that the C state is predissociative and hence gives rise to larger linewidths than the D state.

The experiment yields rotational distributions in terms of J, the total angular momentum quantum number. To make direct comparison with the computational results these have been converted to give distributions in terms of j. To achieve this, Hund's coupling case (b) has been invoked as the spin-orbit coupling constant for NO is small (123 cm^{-1}[46]) and the degree of rotational excitation is high.

The R_1 and R_2 branches of the D $\leftarrow$ X transition in NO were probed between 368.9 and 371.5 nm (equivalent to 3.34 to 3.36 eV). Rotational distributions for both spin-orbit states of NO are shown in panel b) of Figure 9 with those from the R_1 branch ($^2\Pi_{1/2}$) marked by circles and those from the R_2 branch ($^2\Pi_{3/2}$) marked by triangles. Both distributions have similar FWHM values of about Δ_j=9, with the R_1 distribution centred at j=46 and the R_2 centred a little lower at j=44. These results are overlaid with the calculated distribution for this small energy range, given in the figure as a solid line. The calculated distribution peaks at j=45 and has a FWHM of Δ_j=9.5.

The distributions resulting from the Q_1 ($^2\Pi_{1/2}$, circles) and Q_2 ($^2\Pi_{3/2}$, triangles) branches of the C $\leftarrow$ X transition between 376.6 and 378.7 nm (3.27 to 3.29 eV) are plotted in panel d) of Figure 9. Because of the pre-dissociative nature of the C state the distributions are noisier than those for the D state, but still exhibit similar features. The width of the distributions are similar to those for the D state, $\sim \Delta_j$=8-9 and the Q_2 distribution is shifted a little lower than that for the Q_1 branch, being centred at $\sim j$=44 as opposed to $\sim j$=45. The calculated distribution for the C state energy range (solid line) has a peak at j=44 and a FWHM of Δ_j=9.5.

5 Discussion

Experimental and computational NO rotational distributions have been presented in Figure 9: despite some noise in the experimental distributions it is evident that the agreement between the two is very good. The theory recreates the overall shape and widths of the distributions well, with the maxima of the rotational distributions agreeing to within 1-2 quanta. The energy difference between the C and D state transitions is small, but nonetheless appears

to cause a shift in the NO rotational distribution of ∼1 quanta towards higher j for the shorter-wavelength D state. The signal to noise in the experimental results is not sufficient to confirm this effect, but the corresponding shift in the calculated distributions suggests it is real. In addition, the experimental results suggest that the rotational distributions arising from the excited spin-orbit state of NO, $^2\Pi_{3/2}$, are shifted 1-2j higher than those from its ground $^2\Pi_{1/2}$ state, an observation that may be qualitatively explained on energetic grounds.

Previous studies on the photodissociation of the 2 ^{1}A′ state of ClNO have been carried out at the slightly lower wavelength of 355 nm. Our computational results at the equivalent energy predict an NO rotational distribution that peaks at j=47 with a shape and FWHM very similar to the distributions presented above. This is in good agreement with the distribution measured by Torres, Pipes and Baugh.[16] The calculation also reproduces the shape of the distribution obtained by Reisler and co-workers, although the calculated peak is a few quanta higher than the measurement.[9] There is very little difference in the distributions in the two NO spin-orbit states in the observations reported by Torres *et al.*, whereas the results reported by Reisler appear to show a slight shift of the NO $^2\Pi_{3/2}$ distribution to lower j, which is similar to what we have observed.

6 Conclusions

New, purely *ab initio* PESs for the 1 and 2 ^{1}A′ states of ClNO have been calculated. No additional parameters have been added to artificially improve the fit to experiment. Wavepacket dynamics calculations modelling dissociation on the 2 ^{1}A′ surface, incorporating the full transition dipole moment function, have been run using the MCTDH method. By analysing the quantum flux passing into a CAP placed in the asymptotic region of the PES the expected vibrational and rotational product distributions in the NO channel have been calculated. NO is produced almost exclusively in its ground vibrational state. The degree of vibrational excitation does however depend weakly on the TDM function, and is overestimated if this is neglected. NO rotational distributions are found to be narrow and peaked at high j.

3D REMPI experiments at photodissociation energies around 370 nm have probed the NO product state distributions via the C ← X and D ← X bands of NO. As a consequence experimental NO rotational distributions have been obtained at two slightly different wavelength regions. The computational NO distributions agree well with experimental distributions from both our group and others, showing that the computational model is a good one.

7 Acknowledgments

KMJ thanks the University of Leeds and the EPSRC (grant code EP/P503868/1) for funding. JM thanks the ICONIC Marie Curie Initial Training Network

(project code 238761) for funding and support. We are very grateful to Prof. Theofanis Kitsopoulos (FORTH, Crete), Dr. Mike Nix (University of Leeds) and Dr. Colin Western (University of Bristol) for helpful discussions.

8 Keywords

nitrosyl chloride, velocity map imaging, multi-configurational time dependent hartree method, potential energy surfaces

References

[1] G. Kistiakowsky, *J. Am. Chem. Soc.*, 1930, **52**, 102.

[2] D. Solgadi, F. Lahmani, C. Lardeux, and J. Flament, *Chem. Phys.*, 1983, **79**, 225–233.

[3] B. Finlayson-Pitts, *Nature*, 1983, **306**(5944), 676–677.

[4] N. T. Form, B. J. Whitaker, and C. Meier, APR 14 , 2008, **41**(7), 074011.

[5] K. M. Jones and B. J. Whitaker, *to be published*.

[6] R. Schinke, M. Nonella, H. Sueter, and J. Huber, *J. Chem. Phys.*, 1990, **93**(2), 1098–1106.

[7] D. Solter, H. Werner, M. Vondirke, A. Untch, A. Vegiri, and R. Schinke, *J. Chem. Phys.*, 1992, **97**(5), 3357–3374.

[8] A. Ogai, A, C. Qian, and H. Reisler, *J. Chem. Phys.*, 1990, **93**(2), 1107–1115.

[9] Y. Bai, A. Ogai, C. Qian, L. Iwata, G. Segal, and H. Reisler, *J. Chem. Phys.*, 1989, **90**(8), 3903–3914.

[10] C. Goodeve and S. Katz, *Proc. R. Soc. A.*, 1939, **172**(A950), 0432–0444.

[11] D. Solgadi, F. Lahmani, C. Lardeux, and J. Flament, *Chem. Phys.*, 1983, **79**(2), 225–233.

[12] G. Busch and K. Wilson, *J. Chem. Phys.*, 1972, **56**(7), 3655.

[13] A. Ogai, C. Qian, L. Iwata, and H. Reisler, *Chem. Phys. Lett.*, 1988, **146**(5), 367–374.

[14] S. Lacombe, M. Loudet, A. Dargelos, and J. Camou, *Chem. Phys.*, 2000, **258**(1), 1–12.

[15] T. Yamashita and S. Kato, *J. Chem. Phys.*, 2004, **121**(5), 2105–2116.

[16] E. Torres, L. Pipes, and D. Baugh, *Faraday Discuss.*, 1999, **113**, 279–290.

[17] H.-J. Werner, P. J. Knowles, G. Knizia, F. R. Manby, M. Schütz, P. Celani, T. Korona, R. Lindh, A. Mitrushenkov, G. Rauhut, K. R. Shamasundar, T. B. Adler, R. D. Amos, A. Bernhardsson, A. Berning, D. L. Cooper, M. J. O. Deegan, A. J. Dobbyn, F. Eckert, E. Goll, C. Hampel, A. Hesselmann, G. Hetzer, T. Hrenar, G. Jansen, C. Köppl, Y. Liu, A. W. Lloyd, R. A. Mata, A. J. May, S. J. McNicholas, W. Meyer, M. E. Mura, A. Nicklass, D. P. O'Neill, P. Palmieri, D. Peng, K. Pflüger, R. Pitzer, M. Reiher, T. Shiozaki, H. Stoll, A. J. Stone, R. Tarroni, T. Thorsteinsson, and M. Wang, Molpro, version 2010.1, a package of ab initio programs, 2010.

[18] P. J. Knowles and H.-J. Werner, *Chem. Phys. Letters*, 1985, **115**, 259–267.

[19] H.-J. Werner and P. J. Knowles, *J. Chem. Phys.*, 1985, **82**, 5053.

[20] P. J. Knowles and H.-J. Werner, *Theor. Chim. Acta*, 1992, **84**, 95–103.

[21] U. Manthe, H.-D. Meyer, and L. S. Cederbaum, *J. Chem. Phys.*, 1992, **97**, 3199–3213.

[22] H.-D. Meyer, U. Manthe, and L. S. Cederbaum, *Chem. Phys. Lett.*, 1990, **165**, 73–78.

[23] G. A. Worth, M. H. Beck, A. Jäckle, and H.-D. Meyer , The MCTDH Package, Version 9.0, (2012). H.-D. Meyer. See http://mctdh.uni-hd.de.

[24] M. H. Beck, A. Jäckle, G. A. Worth, and H.-D. Meyer, *Phys. Rep.*, 2000, **324**, 1–105.

[25] J. Light and T. Carrington, *Adv. Chem. Phys.*, 200, **114**, 263–310.

[26] A. Jäckle and H.-D. Meyer, *J. Chem. Phys.*, 1998, **109**, 3772.

[27] A. Jäckle and H.-D. Meyer, *J. Chem. Phys.*, 1996, **104**, 7974.

[28] R. Kosloff and D. Kosloff, *J. Comput. Phys.*, 1986, **63**, 363.

[29] C. Leforestier and R. Wyatt, *J. Chem. Phys.*, 1982, **78**, 2334.

[30] A. Jäckle and H.-D. Meyer, *J. Chem. Phys.*, 1996, **105**, 6778.

[31] ed. B. J. Whitaker, *Imaging in molecular dynamics, technology and applications*, Cambridge University Press, 2003.

[32] I. Wilkinson *Some remarks on the photophysics of nitrogen dioxide* PhD thesis, University of Leeds, 2009.

[33] I. Wilkinson and B. J. Whitaker, *J. Chem. Phys.*, 2008, **129**, 154312.

[34] A. Schmaunz, U. Kensy, A. Slenczka, and B. Dick, *Phys. Chem. Chem. Phys.*, 2009, **11**, 7115–7119.

[35] D. Townsend, M. Minitti, and A. Suits, *Rev. Sci. Instrum.*, 2003, **150**, 2530–2539.

[36] G. Cazzoli, C. Esposti, P. Palmieri, and S. Simeone, *J. Mol. Spectrosc.*, 1983, **97**, 165–185.

[37] J. Demaison, A. G. Császár, and A. Dehayem-Kamadjeu, *J. Phys. Chem. A*, 2006, **110**, 1360913617.

[38] A. Ticktin, A. Bruno, U. Bruhlmann, and J. Huber, *Chem. Phys.*, 1988, **125**(2-3), 403–413.

[39] A. Hallou, L. Schriver-Mazzuoli, A. Schriver, and P. Chaquin, *Chem. Phys.*, 1998, **237**(3), 251–264.

[40] E. Heller, *Acc. Chem. Res.*, 1981, **14**, 368–375.

[41] V. Engel, *Chem. Phys. Lett.*, 1992, **189**, 76–78.

[42] M. Brook and J. Kaplan, *Phys. Rev.*, 1954, **96**, 1540–1542.

[43] M. Hippler and J. Pfab, *Mol. Phys.*, 1998, **94**, 313–323.

[44] A. S.-C. Cheung, A. L. Wong, D. H.-Y. Lo, K. W.-S. Leung, K. Yoshino, A. P. Thorne, J. E. Murray, T. Imajo, K. Ito, and T. Matsui, *J. Chem. Phys.*, 2003, **119**, 8373–8378.

[45] C. M. Western , PGOPHER, a Program for Simulating Rotational Structure, http://pgopher.chm.bris.ac.uk.

[46] M. Chase, C. Davies, J. Downey, D. Frurip, R. McDonald, and A. Syverud NIST JANAF Thermochemical Tables. See http://kinetics.nist.gov/janaf/, 1985.

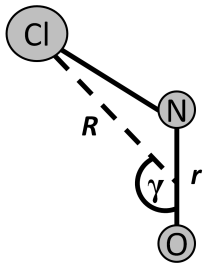

Figure 1: The Jacobi coordinates used in this work. r is the NO bond-length and R is the radial distance from the Cl atom to the centre of mass of the NO moeity. γ is the angle between $\underline{r}$ and $\underline{R}$, also known as the Jacobi scattering angle.

Table 1: The proportion of the total flux going into each product NO vibrational state

NO v	% of total with TDMs	% of total without TDMs
0	91.2	78.9
1	8.3	17.4
2	0.38	3.1
3	0.11	0.53
4	0.04	0.09

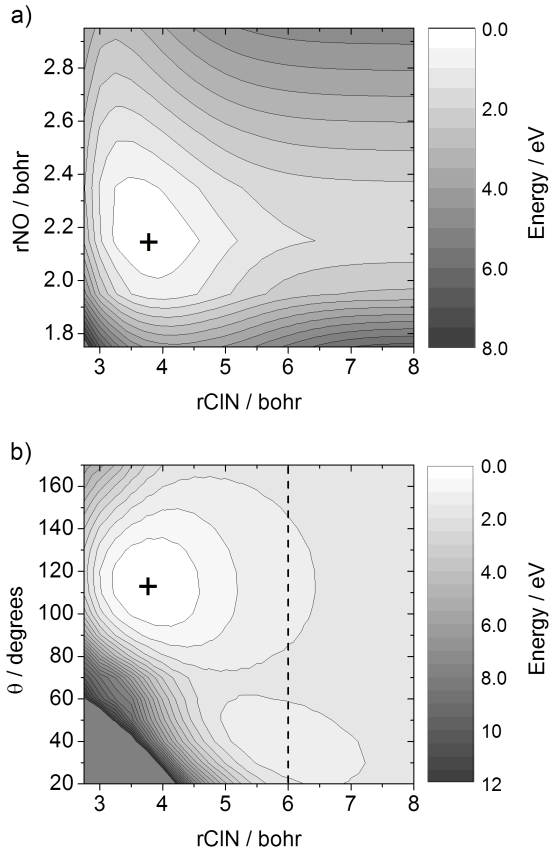

Figure 2: a) A cut through the 1 ^{1}A$'$ surface at a constant angle θ of 110°, scanning the rClN and rNO bond coordinates. b) A cut through the 1 ^{1}A$'$ surface at a constant rNO bond length of 2.15 bohr, scanning the θ and rClN coordinates. The dashed line marks the position of the 1D cut shown in Figure 3. Contour lines are given every 0.5 eV relative to the energy minimum. The crosses mark the minimum energy geometry on each panel.

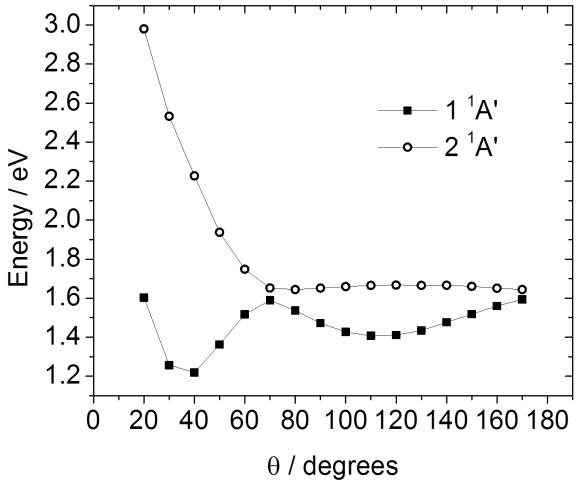

Figure 3: A cut through the 1 (squares) and 2 (circles) $^1A'$ surfaces close to the asymptotic region at a constant rNO bond length of 2.15 bohr and a constant rClN bond length of 6 bohr. Note the interaction between the two states at around θ=70°.

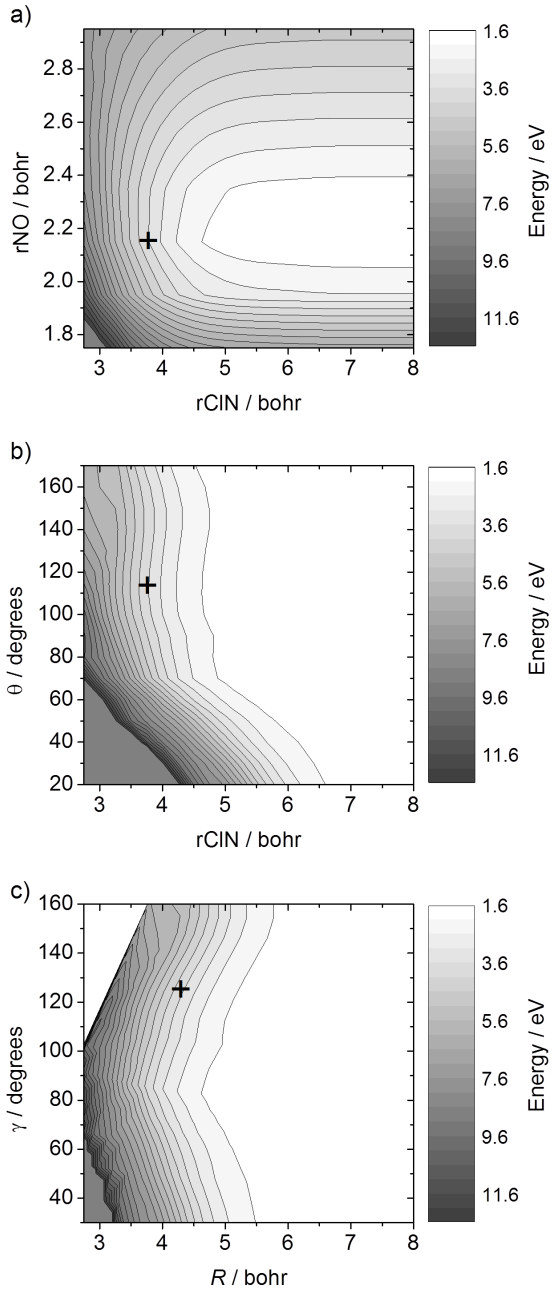

Figure 4: a) A cut through the 2 ^{1}A$'$ surface at a constant angle θ of 110°, scanning the RClN and rNO bond coordinates. b) A cut through the 2 ^{1}A$'$ surface at a constant rNO bond length of 2.15 bohr, scanning the θ and rClN coordinates. c) A cut through the 2 ^{1}A$'$ surface at a constant rNO bond length of 2.15 bohr scanning the Jacobi coordinates γ and R (as defined in Figure 1). Contour lines are given every 0.5 eV relative to the asymptotic energy of 1.6 eV. The crosses mark the approximate Franck-Condon point on each panel.

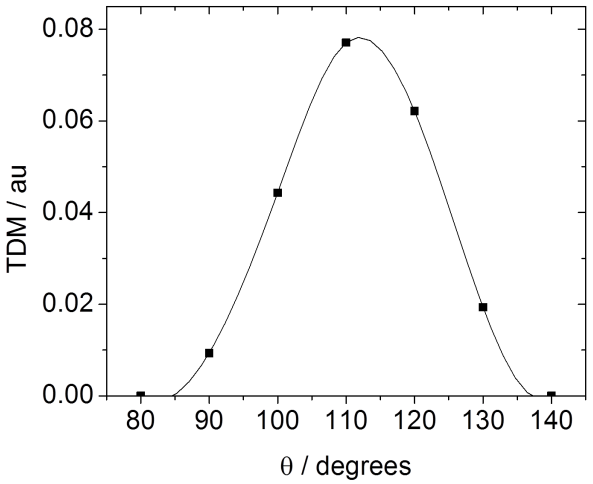

Figure 5: The resultants of the TDM components (given in atomic units) in the molecular plane at various angles for a fixed rNO bond length of 2.15 bohr and a fixed rClN bond length of 3.75 bohr. The connecting line is a spline-fit to guide the eye.

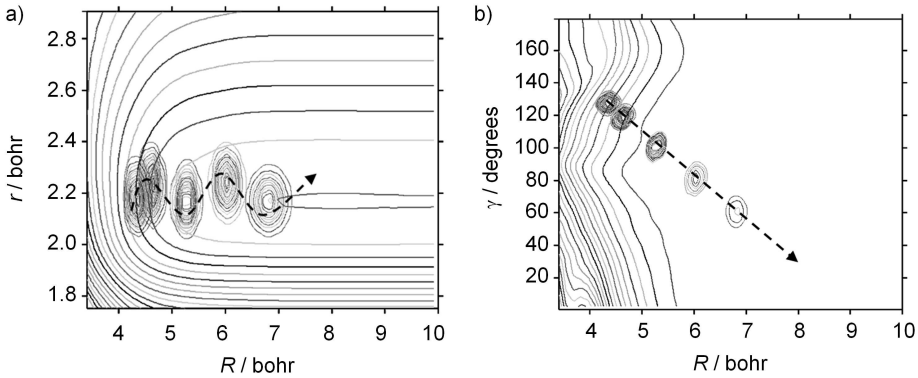

Figure 6: Snapshots of the wavepacket propagation on the $2\ ^1\mathrm{A}'$ state of ClNO, a) for a constant γ of 127° and b) for a constant rNO bond length of 2.15 bohr. Jacobi coordinates are used. The wavepackets are shown at 0, 10, 20, 30 and 40 fs after excitation. The dotted arrows reflect the wavepacket's path. Contour lines on the surfaces are 0.5 eV apart.

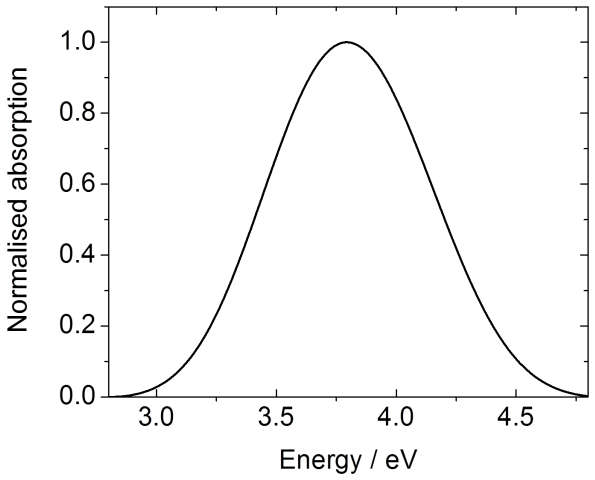

Figure 7: The absorption spectrum calculated via Fourier transformation of the autocorrelation function obtained from a wavepacket propagation on the 2 ^{1}A$'$ state of ClNO. The peak is at an energy of 3.79 eV, equivalent to 327 nm.

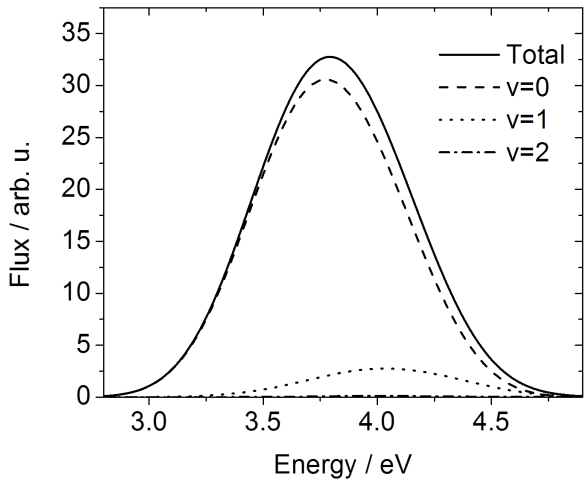

Figure 8: The energy distributions of the total quantum flux, and that going into each product NO vibrational state obtained from a wavepacket propagation on the 2 ^{1}A$'$ state of ClNO. The distributions are broad and featureless, with the peaks shifted slightly in energy for each vibrational state. The majority of NO is formed in v=0.

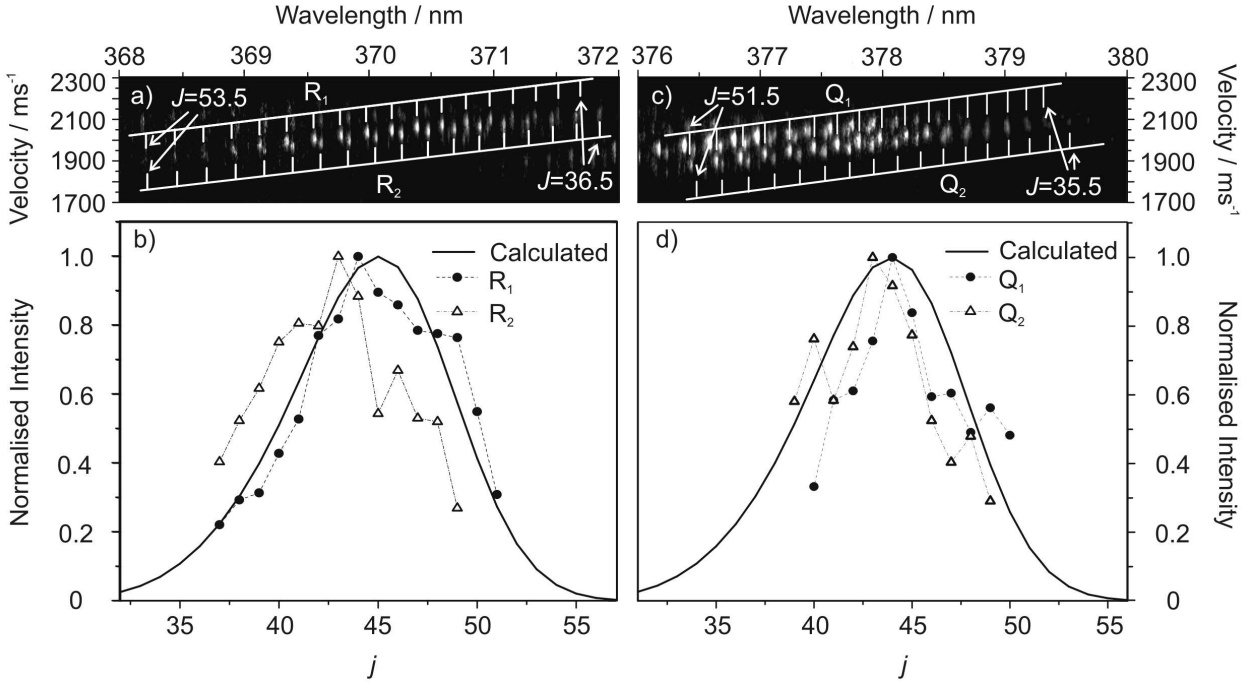

Figure 9: 3D REMPI spectra and comparison of calculated and experimental NO rotational distributions. Panel a) shows the experimental map of wavelength, photofragment velocity and intensity across the range 368.9 to 371.5 nm, which spans the R_1 and R_2 branches of the two-photon D $\leftarrow$ X transition in NO. Rotational combs are overlaid, showing the assigned value of J for each peak, the intensities of which are extracted and presented in panel b), where normalised NO rotational distributions for both the R_1 (circles) and R_2 (triangles) branches are compared with the calculated distribution (solid line). Similarly, panel c) shows the spectrum for the wavelength region including the Q_1 and Q_2 branches of the C $\leftarrow$ X transition in the range 376.6 to 378.7 nm. Panel d) shows the NO rotational distributions extracted from each of the peaks in the assigned Q_1 (circles) and Q_2 (triangles) branches, again compared with the calculated distribution (solid line).